Spanwise Variation in the Unsteady Stalling Flowfields of Two-Dimensional Airfoil Models

Andy P. Broeren* and Michael B. Bragg†
University of Illinois at Urbana—Champaign, Urbana, Illinois 61801

Recent investigations of two-dimensional airfoil stalling characteristics have revealed low-frequency and highly unsteady flow in some cases and large-scale three-dimensional structures in other cases. The latter were referred to as "stall cells" and can form on two-dimensional configurations where the ends of the airfoil model are flush with tunnel side walls or end plates. This paper presents results of detailed investigations of the stalling characteristics of several airfoils that exhibited both low-frequency unsteadiness and large-scale three-dimensional structures. The airfoils were wind-tunnel tested in a two-dimensional configuration. The primary measurements were spanwise wake velocity and mini-tuft flow visualization. The results showed that airfoils with trailing-edge separations at and above maximum lift (static stall) exhibited stall-cell patterns. Conversely, airfoils that had leading-edge separation bubbles that grew in size as the angle of attack was increased into stall developed the low-frequency, highly unsteady flow. This unsteadiness was found to be essentially two dimensional. Therefore, the development of either of these phenomena appears to be determined by the characteristics of the boundary-layer separation leading up to the stall.

Nomenclature

b	=	model span
C_l	=	mean lift coefficient, $L/q_\infty cb$
$C_{l,max}$	=	maximum lift, coincident with α_{stall}
$C'_{l,rms}$	=	rms of the fluctuating lift coefficient
c	=	airfoil chord
E	=	mean hot-film wake-velocity voltage
E'_{rms}	=	rms of the fluctuating hot-film wake-velocity voltage
f	=	flow oscillation frequency
L	=	mean airfoil lift
q_∞	=	freestream dynamic pressure
Re	=	Reynolds number based on chord, $\rho U_\infty c/\mu$
Sr	=	Strouhal number, $fc \sin\alpha/U_\infty$
U_∞	=	freestream velocity
x	=	distance in streamwise direction
y	=	distance in spanwise direction
α	=	angle of attack
α_{stall}	=	stalling angle of attack, coincident with $C_{l,max}$
μ	=	absolute air viscosity
ρ	=	air density
ϕ	=	phase angle

Introduction

THE stalling of airfoils is a complex fluid dynamic phenomenon involving strong viscous-inviscid interaction, boundary-layer separation, and unsteady flow. There are various reports of unsteadiness associated with airfoil stall in the technical literature. One study in particular describes a low-frequency, large-scale unsteady flow. Zaman et al.[1] performed a detailed investigation into this naturally occurring, quasi-periodic phenomenon. The flow oscillation frequencies measured in the airfoil wake were nondimensionalized using the freestream velocity and the airfoil projected height ($c \sin\alpha$). The resulting Strouhal numbers were on the order of 0.02, approximately 10 times lower than those associated with bluff-body shedding or a von Kármán vortex street. This low-frequency oscillation occurred in the range of static stall, or maximum lift, from $\alpha \approx 14.5$ to 16.5 deg and involved a quasi-periodic switching of the

flow between stalled and unstalled conditions. This resulted in large-amplitude force fluctuations, up to 50% of the mean lift coefficient at 15-deg angle of attack. Curiously, this low-frequency oscillation completely diminished as the angle of attack was increased, with bluff-body shedding frequencies (i.e., $Sr \approx 0.2$) being measured at $\alpha = 18$ deg.

Research into this low-frequency oscillation on the LRN-1007 airfoil was subsequently performed by others,[2−7] and the features of the unsteady phenomenon are well known. The study of Zaman et al.[1] was conducted for Reynolds numbers less than 1×10^5, and Bragg et al.[5] extended this range up to 12.5×10^5 and measured the oscillation frequency at 12 angles of attack from 14.4 to 16.6 deg. The Strouhal number varied from 0.017 to 0.30 and had very little dependence on Reynolds number but had a very strong dependence on angle of attack. In the same paper Bragg et al.[5] also provided surface oil-flow visualization results obtained for the LRN-1007 airfoil prior to the onset of the unsteady flow. There was a leading-edge separation bubble that grew in size on the upper surface as the angle of attack was increased. The data also showed that there was significant boundary-layer separation from a point downstream of the separation bubble reattachment. The photographs of this flow visualization revealed that these features were uniform across the span of the airfoil model.[4] However, the oil-flow visualization results were essentially time-averaged. The separation bubble was found to play a key role in the oscillation, as its elimination (with a boundary-layer trip) caused the low-frequency oscillation to vanish.[4,5]

The role of the separation bubble and turbulent boundary-layer (or trailing-edge) separation was investigated in more detail by Broeren and Bragg.[7] They performed LDV (laser Doppler velocimeter) measurements on the LRN-1007 airfoil upper surface for $\alpha = 15$ deg and $Re = 3 \times 10^5$. The authors were able to conditionally average the time-dependent velocity data using the wake velocity as the synchronization source because the naturally occurring flow oscillation was nearly periodic for this case. The result was a quantitative description of the upper surface flowfield over an averaged oscillation cycle. The data showed the development and growth of a leading-edge separation bubble that merged with the turbulent boundary-layer separation causing a completely separated or stalled condition. Although this study revealed key information about the low-frequency oscillation, the LDV measurements were only performed for a single two-dimensional plane at the model midspan. Therefore, no information about the spanwise, or three-dimensional, character was obtained. This may be an important factor as other studies have documented large-scale three-dimensional features in the flowfields of stalled airfoils.

There has been a significant amount of research focused on three-dimensional structures known as stall cells. These

---

mushroom-shaped patterns form from strong recirculating flows on stalled airfoil models and wings. Winkelmann and Barlow[8] noted that the stall cells formed on both two-dimensional models where the ends of the model are flush with tunnel side walls or splitter plates and on plane rectangular wings of finite aspect ratio. The stall cells began to form as the angle of attack was increased into maximum lift and existed on the surface several degrees above the stalling angle of attack. The authors sketched a tentative flowfield model showing the general features of a leading-edge separation bubble and trailing-edge separation. These features are qualitatively similar to that just described for the LRN-1007 airfoil operating near stall. The authors pointed out that this flowfield was probably unsteady in nature, but their oil-flow visualization method produced only time-averaged results. Winkelmann[9] measured the fluctuating velocity spectra in the wake of a rectangular wing model, and his results did not show any evidence of low-frequency components.

The unsteady features of stall cells were later addressed by Yon and Katz,[10] who used fine-thread tuft-flow visualization and high-frequency response pressure transducers for measurements on a NACA 0015 airfoil model of variable aspect ratio. The variable aspect ratio model was equipped with end plates that effectively eliminated the tip flow resulting in essentially a two-dimensional configuration. The authors discovered that certain aspect ratios resulted in noninteger numbers of stall cells that were characteristically unsteady. The power spectra of their unsteady pressure measurements showed evidence of low frequencies on the same order as those measured for the LRN-1007 airfoil. However, the intensity of this unsteadiness was apparently not as severe. In this case maximum lift (or stall) occurred at approximately 16 deg, with the stall-cell patterns being visible in the range of 17- to 19-deg angle of attack.

The objective of the present paper is to show that there is a fundamental difference in the stalling character of airfoils exhibiting three-dimensional flowfield variations vs airfoils exhibiting low-frequency unsteady flow. That is, it will be shown that the low-frequency oscillation as described for the LRN-1007 airfoil is essentially two-dimensional. The role of the stall-cell structures in steady-stall cases is also addressed. The unsteady flow described for the LRN-1007 airfoil is not an anomaly and is shown to occur for other airfoils. Several experimental methods were employed to accomplish these objectives. Spanwise velocity measurements were carried out using a traversable probe in the airfoil wake. These quantitative measurements were supplemented with mini-tuft surface flow visualization data. A novel method of conditionally averaging the mini-tuft data was developed to facilitate analysis of the unsteady stall cases.

Experimental Methods

All experiments were carried out at the University of Illinois Subsonic Aerodynamics Laboratory using the low-speed, low-turbulence wind tunnel. The general experimental arrangement is shown in Fig. 1. The 12-in. (30.48-cm) chord wind-tunnel models spanned the test section vertically, a distance of 33.63 in. (85.42 cm). The width of the test section was 48 in. (122 cm) so that this model orientation minimized the blockage and facilitated flow visualization because photographs were taken from the side. All data were acquired at a Reynolds number of 3×10^5 because this corresponded to previous measurements.[6] A traversable hot-film probe was used to measure the wake velocity at 15 spanwise stations: one at midspan and seven stations above and below midspan. The probe location in the wake also corresponded to the location used for the conditionally averaged LDV measurements.[6,7] The use of the terms "above" and "below" are convenient to use given the vertical orientation of the model but should not be taken literally because this model orientation is arbitrary. Several pieces of information were gleaned from the wake-velocity data. The power spectra were obtained using a dynamic signal analyzer, and the Strouhal numbers were computed. The mean and rms of the fluctuating velocity voltage were also computed.

A rigorous uncertainty analysis was carried out using the methods of Kline and McClintock[11] and Coleman and Steele[12] for 20:1 odds. The wake hot-film probe was not calibrated to output velocity,

Airfoil chord = c = 12.00 in. (30.48 cm)
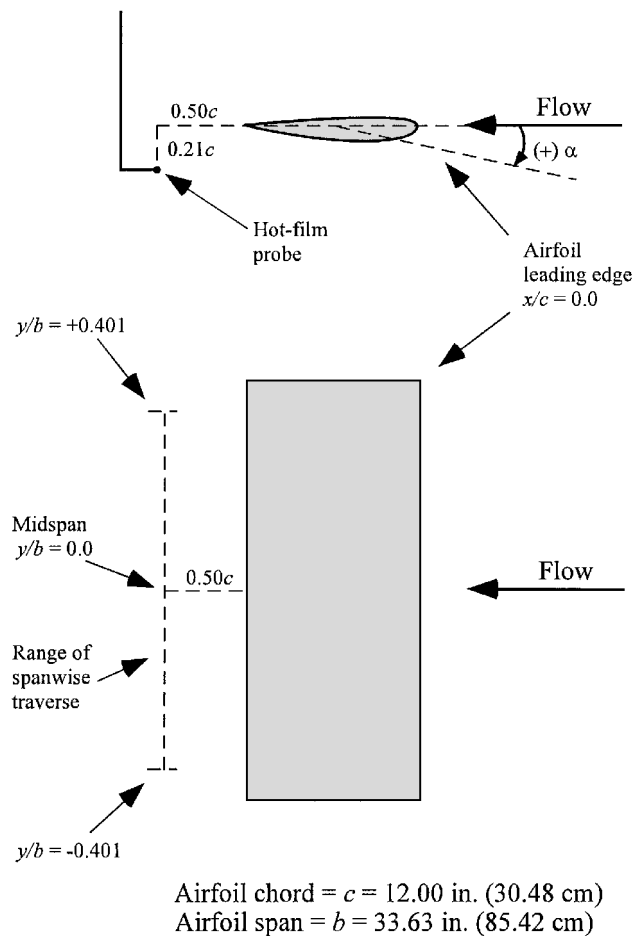Airfoil span = b = 33.63 in. (85.42 cm)

Fig. 1 Schematic drawing showing the experimental arrangement for the wake-velocity measurements.

and so only the voltages are reported here. These voltages were acquired using a 16-bit analog-to-digital conversion board that had a rated accuracy of $\pm 0.76\,\mu$V. Because the wake voltages were on the order of unity, the relative uncertainty was nearly 0%. The quantization error was 0.153 mV; however, the mean and rms voltage were sufficiently resolved through the acquisition of 30,000 samples. The Strouhal number was computed from the frequency spectrum, the angle of attack, the airfoil chord, and the freestream velocity. The absolute uncertainty in angle of attack was ± 0.05 deg. This and the uncertainties in the other quantities (f, U_∞) led to a relative uncertainty in the Strouhal number of $\pm 2.5\%$. More details regarding the uncertainty analysis can be found in Broeren.[13]

In addition to the wake-velocity measurements, flow visualization was performed using fluorescent mini-tufts.[14] The mini-tufts consisted of 0.002-in. (0.05-m)-diam monofilament nylon that were dyed fluorescent. This caused the tufts to fluoresce under UV illumination. The small size of the tufts limited their effect on the boundary-layer flow and provided excellent frequency response for the unsteady cases. The tufts were able to capture the key features of the unsteady flowfields over stalled airfoils. Although detailed boundary-layer information was not obtainable, general patterns of separation and reattachment were recognizable. The tufts were applied to the entire model surface so that spanwise variations in these features could also be ascertained. The mini-tuft flow visualization data were processed in a rather unique way to yield information about the spanwise variation of the flowfield near the surface of the airfoil. The hot-film sensor, positioned at midspan, was used as a synchronization signal for the acquisition of mini-tuft photography. That is, a computer algorithm sampled the wake-velocity voltage signal and triggered the shutter of a camera at designated points during each oscillation of the flow. This was not only possible, but quite effective, because the unsteadiness was very nearly periodic. The photographs were ordered and sorted into time slots (or bins)
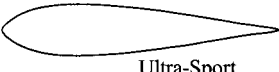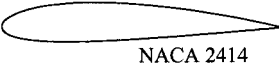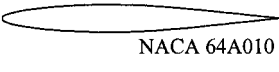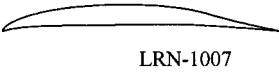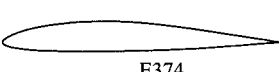
	THICKNESS	CAMBER
Ultra-Sport	18.6%	0.00%
NACA 2414	14.0%	2.00%
NACA 64A010	10.0%	0.00%
LRN-1007	7.3%	5.90%
E374	10.9%	2.24%

Fig. 2   Airfoils tested.

based on their phase-locked relationship. The phase angle ϕ was used to represent the time designation within each cycle. (Note that the phase angle is perhaps best defined by the description of Fig. 14 in the Discussion section.) Each time slot (or bin) was approximately 15 to 20 deg of the 360-deg cycle. The actual width of each slot depended upon the grouping of the photographs.

There were 15 chordwise rows of mini-tufts on the model, placed at spanwise locations coincident with the wake-velocity measurements just described. Each row in each photograph was analyzed to determine the approximate locations of flowfield features such as separation bubble reattachment or boundary-layer separation. The estimated uncertainty in determining boundary-layer separation features in the mini-tuft patterns was ±10% chord, or less, and ±5% chord for bubble reattachment locations. The chordwise locations of these features were tabulated and then averaged with the data from the other photographs in each of their respective time slots. This method produced information about the unsteady flowfield averaged over an oscillation cycle.

A total of five airfoils were tested in this study and are shown in Fig. 2 along with their corresponding thickness and camber. The airfoils encompassed a broad range of stall behavior and were selected to illustrate the differences in the stalling behavior. More details regarding the experimental methods, data reduction, and uncertainty can be found in Broeren.[13]

Results

Review of Time-Dependent Lift Data

Time-dependent lift data were acquired for several airfoils having different stalling characteristics, and these results are presented and discussed by Broeren and Bragg.[15,16] Five of these airfoils were selected for more detailed study and are considered here. The mean lift coefficient C_l and rms of the fluctuating lift $C'_{l,\mathrm{rms}}$ data are presented in Fig. 3. Of particular interest here is the stalling behavior of these airfoils. The heavy vertical lines near stall in each plot indicate the range for which the salient flowfield features were observed. For the Ultra-Sport and NACA 2414 airfoils, stall-cell structures, similar to those just described, were observed over the indicated range. For the NACA 64A010, E374, and LRN-1007 airfoils, stall cells were not observed; instead low-frequency unsteady flow characterized the stall. The remainder of this paper presents the major differences in these flowfields and intends to show that they exist exclusively, that is, they do not appear to coexist.

Before presenting these arguments in detail, some discussion of the airfoil data in Fig. 3 is warranted. These five airfoils represent four different stall types. Time-averaged stalling characteristics can be divided into three fundamental types based upon the flowfield development leading up to the stall. It is common for airfoils to exhibit a combination of these features, thus resulting in more than the three basic types. McCullough and Gault[17] performed systematic testing and formulated the present definitions and understanding of airfoil stall type. The Ultra-Sport airfoil (Fig. 3a) had a classic trailing-edge stall type. That is, the boundary-layer separation location gradually

moved forward on the airfoil as the angle of attack was increased into stall. The NACA 2414 airfoil had characteristics of the leading-edge stall type. In this case the stall occurred as a result of abrupt flow separation from the leading edge, without subsequent reattachment. The result was a discontinuous loss of lift as illustrated in Fig. 3b. For this stall type a small laminar separation bubble formed near the leading edge, and the "abrupt" flow separation likely resulted from the "bursting" of this bubble. This airfoil also exhibited aerodynamic hysteresis as the mean lift was not fully recovered until the angle of attack was decreased below stall. This lift hysteresis is fairly well known (e.g., see Ref. 18), and the present data reveal a similar trend in the fluctuating lift $C'_{l,\mathrm{rms}}$. The third basic stall type is thin-airfoil stall. This stall type is characterized by boundary-layer separation from the leading edge with reattachment (a separation bubble) at a point that moves progressively aft on the airfoil upper surface as the angle of attack is increased into stall. The effect of this large bubble is shown in Fig. 3c for the NACA 64A010 airfoil. There was a distinct reduction in the lift curve slope near $\alpha = 4$ deg associated with the growth of the leading-edge bubble. The gradual stall, at fairly low lift coefficients, is also a hallmark of the thin-airfoil stall type. The remaining two airfoils, the LRN-1007 and the E374, represent a combination of both the thin-airfoil and trailing-edge stall types. That is, both airfoil flowfields exhibited a leading-edge separation bubble that increased in size with angle of attack (characteristic of thin-airfoil stall) and trailing-edge separation that moved forward with increasing angle of attack (characteristic of trailing-edge stall). The relative magnitudes of flow unsteadiness is also revealed in the rms lift variation. The $C'_{l,\mathrm{rms}}$ levels at maximum lift for the Ultra-Sport and NACA 2414 (increasing α) are very low and increase as the angle of attack increases. In contrast, the $C'_{l,\mathrm{rms}}$ for the other airfoils reaches a peak nearly coincident with maximum mean lift, then decreases as the angle of attack increases. Although low-frequency unsteady flow was observed for both the thin-airfoil and combination thin-airfoil and trailing-edge stall types, it was much more pronounced and periodic for the latter combination stall type.

Spanwise Flowfield Data

As just described, the Ultra-Sport airfoil exhibited characteristics of trailing-edge stall, where the turbulent boundary-layer separation point moved forward on the airfoil as the angle of attack was increased into stall. The extent of boundary-layer separation is illustrated in Fig. 4 at $\alpha = 10$ deg, the stalling angle of attack. The orientation of the tufts in the photograph revealed that there was more boundary-layer separation above the midspan location as indicated by the tufts that failed to align themselves in the streamwise direction. In contrast, there were several rows below midspan that indicated separation locations much closer to the trailing edge. The last few tuft rows, near the bottom of the model, showed increased separation. The flow direction is opposite of the standard convention as a result of the orientation of the wind-tunnel facility. Photographs taken at $\alpha = 13$ and 16 deg revealed that the extent of separated flow progressed toward the leading edge. Any flow unsteadiness in this angle-of-attack region was weak and broadband.

A quantitative analysis of the information from the mini-tuft visualizations was performed by determining the boundary-layer separation location for each of the 15 tuft rows. This could be estimated to within $x/c = \pm 0.10$ or better because the tufts were applied in increments of 10% chord. The result of this process is also shown in Fig. 4. The vertical axis of the plot represents the model span; with the midspan location at $y/b = 0.0$, the top of the model is at $y/b = 0.5$, and the bottom of the model is at $y/b = -0.5$ so that the vertical coordinate of each data point represents the spanwise location of the tuft rows. The horizontal axis is the chordwise location of the boundary-layer feature of interest, which is the boundary-layer separation location in this case. The x axis is reversed from that shown in the photograph as the leading edge at $x/c = 0.0$ is now in its usual position on the left. This means that the flow direction implied on the plot is from left to right, opposite that shown in the photograph. The vertical or spanwise direction remains the same. The decision to reverse the x axis was not a deliberate attempt to confuse the reader, but to standardize the plots. The aspect ratio of the plot is identical to the wind-tunnel models, where $b/c = 33.63/12.00 = 2.8$.
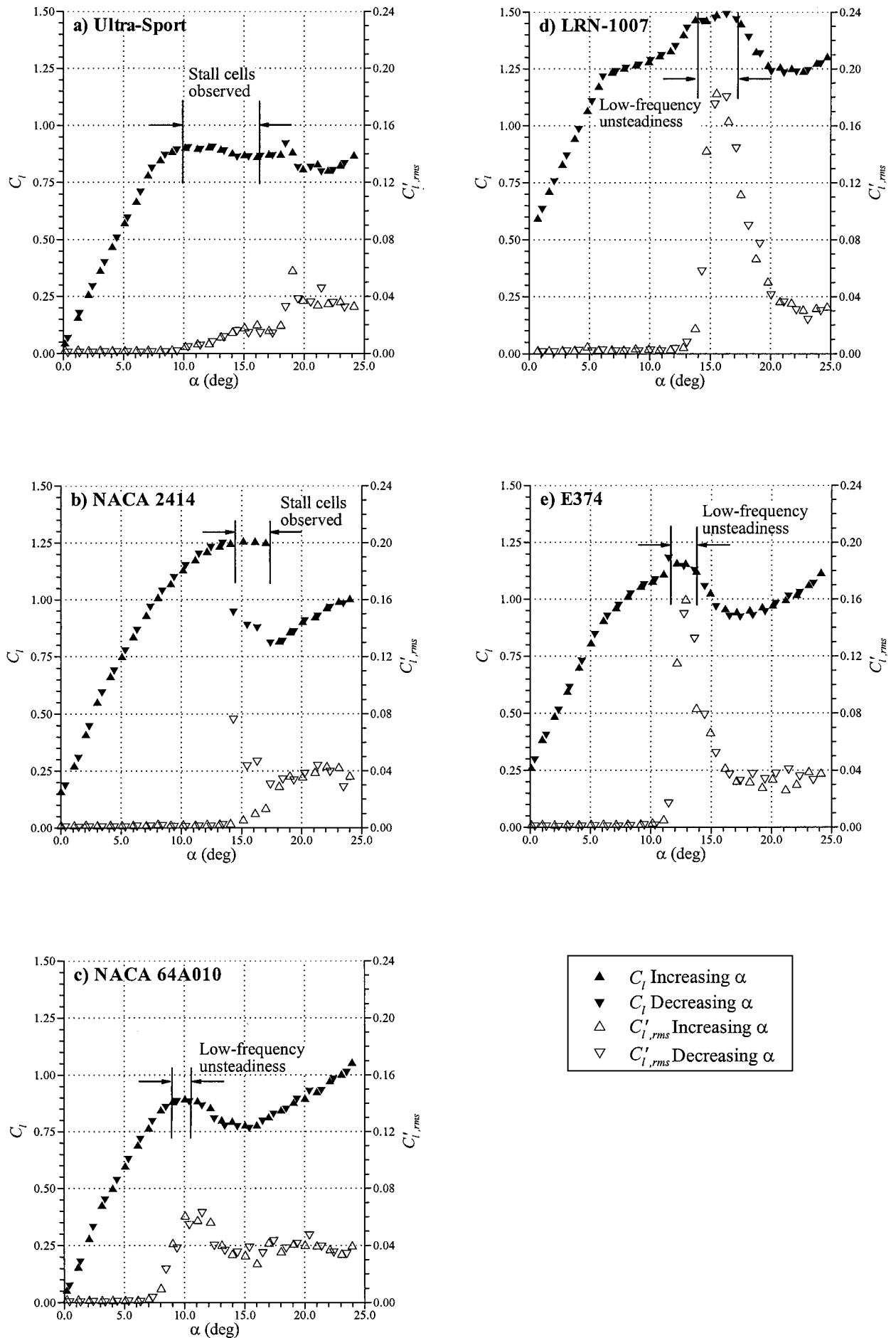
Fig. 3   Mean and fluctuating lift coefficient variation with angle of attack for airfoils with different stall types, after Broeren and Bragg.[15,16]
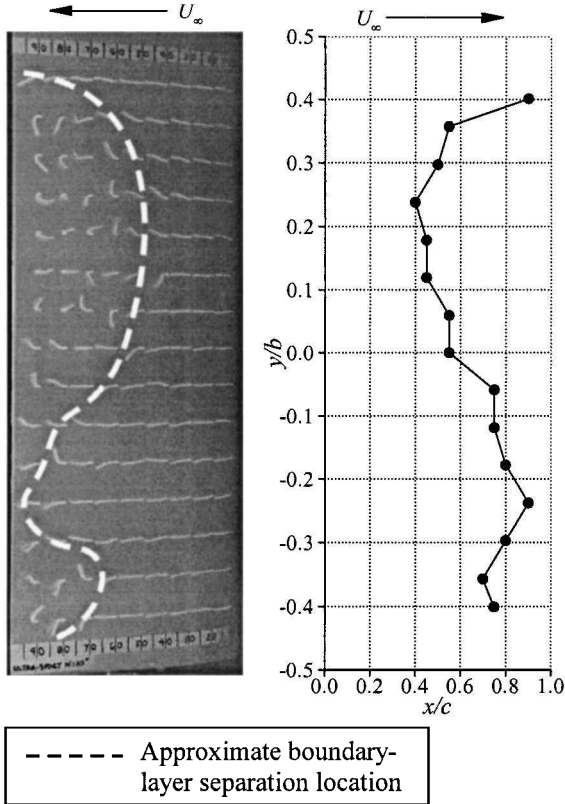
Fig. 4 Photograph at left shows mini-tuft flow visualization patterns on the Ultra-Sport airfoil at $\alpha = 10$ deg. The plot (at right) shows the corresponding boundary-layer separation locations determined from the flow visualization.
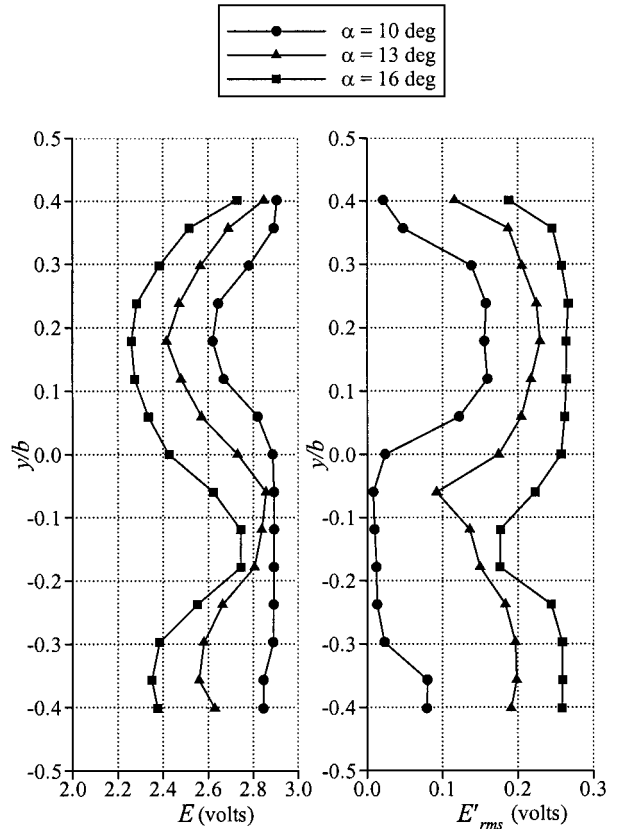

Fig. 5 Spanwise variation in the mean and fluctuating wake-velocity voltage for the Ultra-Sport airfoil.

Fig. 6 Spanwise variation in the boundary-layer separation location determined from the mini-tuft flow visualization for the NACA 2414 airfoil.

The boundary-layer separation locations shown in the plot preserved the spanwise variation observed in the corresponding photograph. The separation locations were close to $x/c = 0.45$ on the upper half of the model for $0.10 < y/b < 0.30$. This is contrasted with the lower half of the model on the interval $-0.18 < y/b < -0.30$, where the separation location was at or downstream of $x/c = 0.80$.

The wake-velocity measurements provided more quantitative results to confirm the spanwise flowfield variations observed in the mini-tuft data. The mean and rms wake-velocity voltages for the Ultra-Sport airfoil are plotted in Fig. 5 for $\alpha = 10$, 13, and 16 deg. Considering the data for $\alpha = 10$ deg, the mean velocity showed a defect centered at approximately $y/b = 0.20$, which coincided with the region of largest boundary-layer separation (cf. Fig. 4). Conversely, the mean wake velocity was larger and more uniform for the region of least boundary-layer separation in the general range of $-0.10 < y/b < -0.30$. These results were complementary because increased boundary-layer separation would lead to a larger wake and hence a larger velocity defect. The rms velocities were also consistent, as there was a minimum at the spanwise location corresponding to the region of the least boundary-layer separation. The mean velocity data for $\alpha = 13$ and 16 deg indicated increased spanwise variation in the flowfield. The large velocity defects for these two cases suggested that the wake became larger as the angle of attack was increased, consistent with boundary-layer separation moving forward on the airfoil. These large spanwise variations indicated that stall-cell structures likely existed on the surface. This is revisited again in the Discussion.

The leading-edge stall-type airfoils were represented by the NACA 2414 as this airfoil clearly exhibited the chief characteristics of this stall type. The mini-tuft flow visualization data, summarized in Fig. 6, were similar to the Ultra-Sport data. There was a larger extent of separated flow above midspan than below, for $\alpha = 15$ and 16 deg. For $\alpha = 17$ deg the boundary layer was completely separated from near the leading edge, and this involved a rapid transition from an unstalled condition. Recall that the key characteristic of this stall type was the leading-edge separation bubble that was thought to have
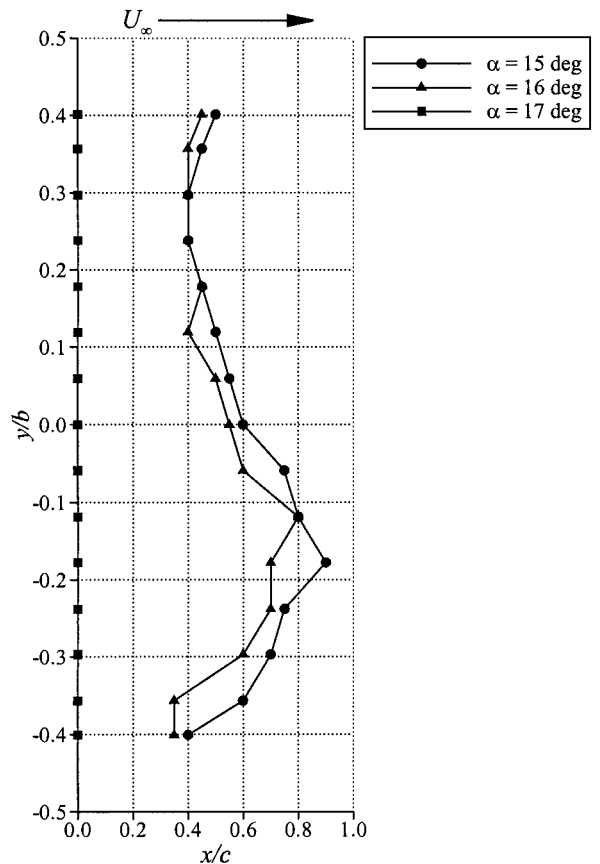
"burst," thus leading to the discontinuous loss of lift (cf. Fig. 3b). The separation bubble was observed in previous surface oil-flow visualizations[13] but could not be observed in the mini-tufts because the reattachment location was upstream of the first row of tufts at $x/c = 0.10$. This abrupt stall was observed while recording the present data. The freestream velocity was set to achieve a Reynolds number of 3×10^5, and the angle of attack was slowly increased from 0 to 17 deg. The flow on the upper surface remained unstalled at $\alpha = 17$ deg for approximately 30 s, then became instantly separated and fully stalled. The lift curve for the NACA 2414 airfoil exhibits aerodynamic hysteresis about $C_{l,\max}$, and it is important to distinguish between increasing angles of attack and decreasing angles of attack. For the purposes of this paper, any angle of attack mentioned in connection with the NACA 2414 airfoil should be taken as one increased from a lesser value, unless stated otherwise.

The wake-velocity data showed spanwise variations corresponding to those shown in the mini-tuft data. Although the data presented for the NACA 2414 and Ultra-Sport airfoils are complementary, they deeply contrast the following results for the remaining airfoils.

The thin-airfoil stall-type category is represented by the NACA 64A010 airfoil. The data presented in this case are slightly different from the data already presented in that the mini-tuft and spanwise velocity results are not shown for analogous angles of attack because this airfoil exhibited low-frequency unsteady flow fluctuations in the range of $8.7 < \alpha < 10.2$ deg, with maximum lift occurring at about 10.1 deg. The mini-tuft images were difficult to interpret in this range owing to the unsteady flow; therefore, these data are for angles of attack leading up the onset of the unsteadiness. On the other hand, the wake-velocity data were acquired for angles of attack beginning at $C_{l,\max}$ and continuing up to the onset of bluff-body shedding.

The key flowfield feature preceding the stall of the NACA 64A010 was the leading-edge separation bubble that grew in size on the airfoil upper surface with increasing angle of attack. The separation bubble reattachment locations determined from the mini-tuft data are shown in Fig. 7. The data reveal how rapidly the separation bubble grew in size from a reattachment at $x/c \approx 0.15$ for $\alpha = 7.4$ deg to reattachment at $x/c \approx 0.50$ for $\alpha = 8.4$ deg. There was significant variation in the reattachment location across the span at $\alpha = 8.4$ deg. Unsteady flow in the reattachment region impeded interpretation of the tuft orientations. The poor chordwise resolution of the tufts also added to this difficulty. In spite of this, the reattachment locations, when averaged across the span, compared very well to previous surface-oil flow visualization results.[13] Finally, the mini-tuft data confirmed previous surface-oil flow results that showed very little turbulent boundary-layer separation downstream of the bubble reattachment.

Spanwise wake-velocity data were collected for angles of attack beginning near $C_{l,\max}$ at $\alpha = 10$ deg and continued into the onset of bluff-body shedding at $\alpha = 15$ deg. The mean and rms velocity voltages for these cases are shown in Fig. 8. Unlike some of the preceding results, these data exhibited more spanwise uniformity. The mean velocities for $\alpha = 12$ and 13 deg showed some retarded flow above the midspan (that was not present later), but the variation was much less than that already observed for the Ultra-Sport and NACA 2414 airfoils. The bluff-body shedding case at $\alpha = 15$ deg, was very uniform in both the mean and rms velocity, consistent with previous data.[13] The mini-tuft images for $\alpha = 10$–13 deg (not shown here) indicated separated flow from the leading edge, which was expected since the airfoil was stalled at these angles of attack.

A key objective of this study was to determine whether the low-frequency flow oscillation occurring on the LRN-1007 airfoil was essentially a two-dimensional phenomenon, or whether there was large spanwise variation in the unsteady flowfield. Spanwise wake-velocity data indicated good uniformity in terms of integrated quantities. For example, Fig. 9 shows the variation in the Strouhal number and power spectra amplitude across the wake for three angles of attack in the low-frequency oscillation range. The Strouhal number was based upon the frequency at the midpoint of the -3 dB bandwidth of the fundamental spectral peak, and the peak amplitude corresponds to the -3 dB level. The Strouhal number was essentially constant across the span, indicating that the fundamental frequency of the oscillation did not vary in this direction. The
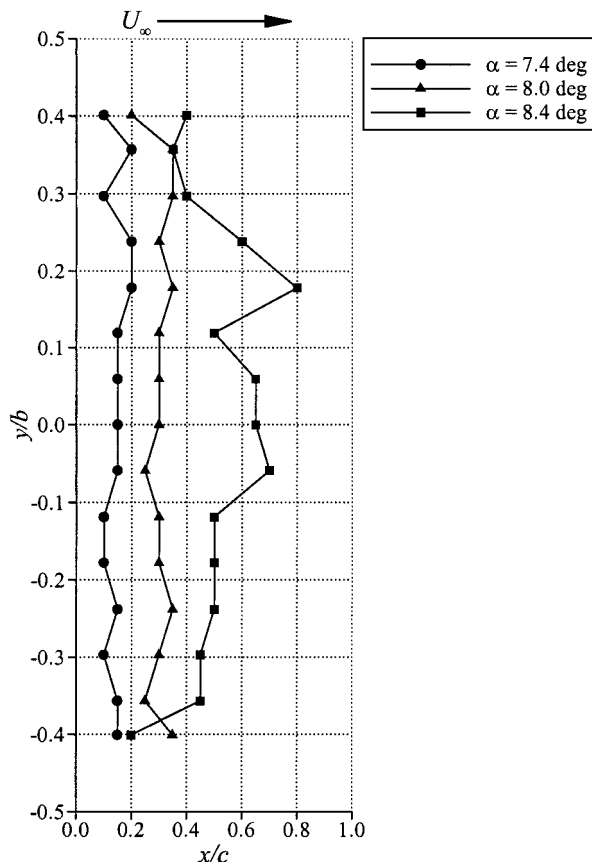

Fig. 7 Spanwise variation in the leading-edge bubble reattachment location determined from the mini-tuft flow visualization for the NACA 64A010 airfoil.
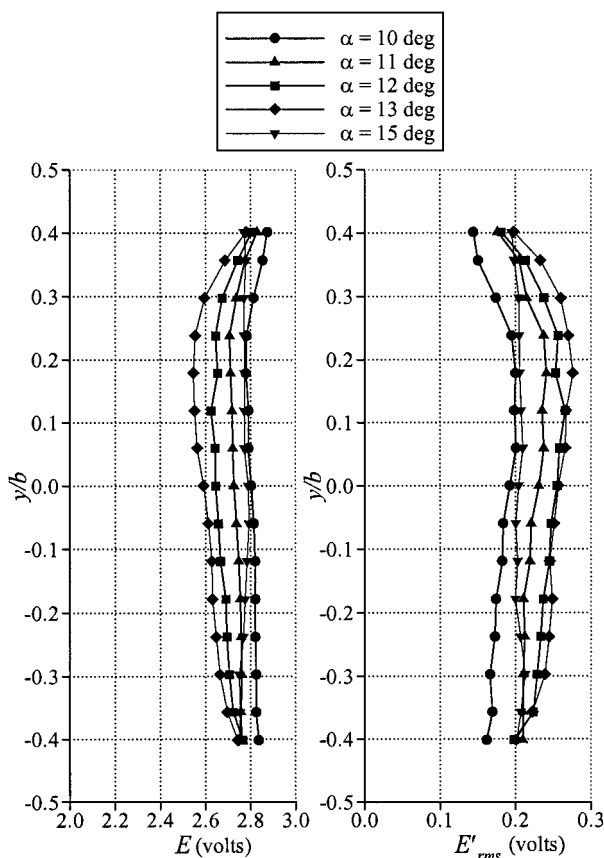

Fig. 8 Spanwise variation in the mean and fluctuating wake-velocity voltage for the NACA 64A010 airfoil.
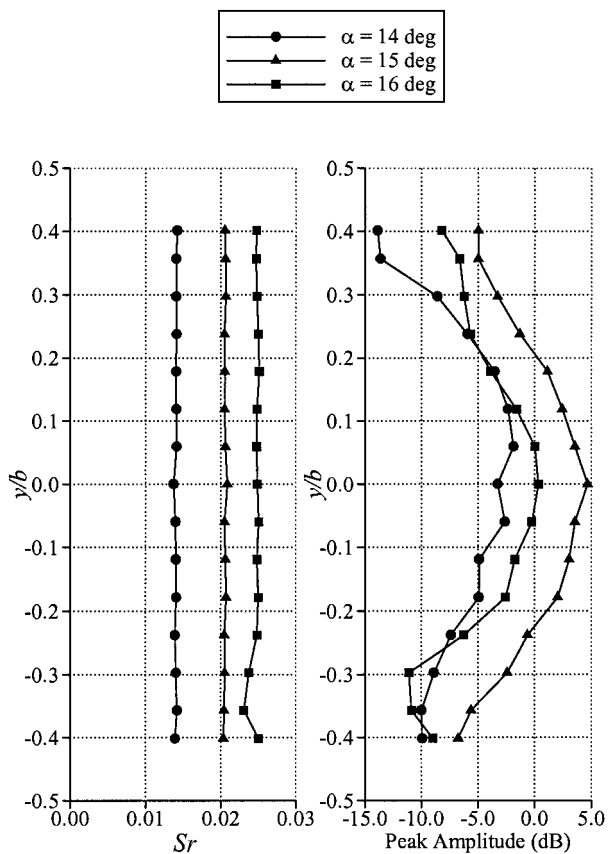
Fig. 9 Spanwise variation in the Strouhal number and peak amplitude determined from the fluctuating wake-velocity voltage for the LRN-1007 airfoil.

increasing Strouhal number with angle-of-attack trend was identified in earlier studies (e.g., Ref. 5) and are in agreement with the present data. The peak amplitude decreased significantly toward the ends of the model. The unsteady flow at each end of the model was likely attenuated by the presence of the tunnel walls. However, the reduction in amplitude across the span was essentially symmetric from midspan.

Similar trends were observed in the wake-velocity voltage and its rms value (see Fig. 10). The mean velocity voltage near the ends of the model was slightly higher than values near the model midspan, likely indicating that the wake was slightly larger at this location (midspan). As expected, the rms values behaved analogously to the peak amplitude variation from Fig. 9. Because the rms voltage was related to the integrated power spectrum amplitude, the similar variation indicated the large contribution of the low-frequency oscillation to the total rms. These trends in the wake-velocity data contrast with the spanwise variation observed for the previous Ultra-Sport and NACA 2414 airfoils.

The conditionally averaged mini-tuft flow visualization results were consistent with the wake-velocity measurements. Figure 11 shows the boundary-layer separation location at various times (or phase angles, ϕ) in the conditionally averaged oscillation cycle. The data shown are for $\alpha = 15$ deg because it had the largest amplitude (cf. Fig. 9) and confirmed that the low-frequency oscillation was most intense near this angle of attack. For each point in the cycle, the boundary-layer separation location was essentially uniform across the span. Furthermore, the separation location moved downstream from an average location at $x/c \approx 0.35$ for $\phi = 40.8$ deg to $x/c \approx 0.80$ for $\phi = 229.2$ deg. During the cycle, a separation bubble formed on the upper surface, and the reattachment location was visible in the mini-tuft patterns. These data are summarized in Fig. 12. The earliest time in the averaged cycle when a definite reattachment pattern became visible was $\phi = 149.0$ deg, with the location at $x/c \approx 0.05$. It was assumed that the bubble separation location was very near the leading edge, which was fairly sharp for the LRN-1007
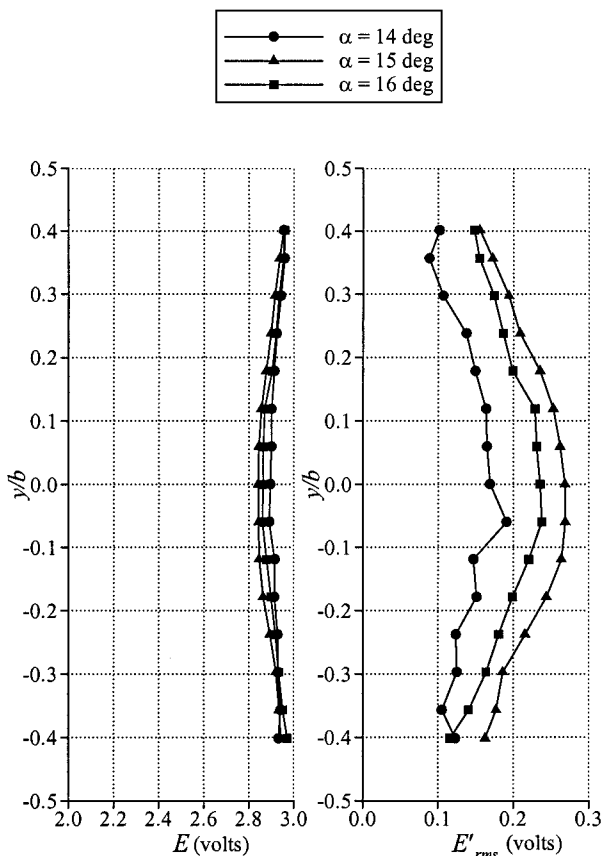

Fig. 10 Spanwise variation in the mean and fluctuating wake-velocity voltage for the LRN-1007 airfoil.
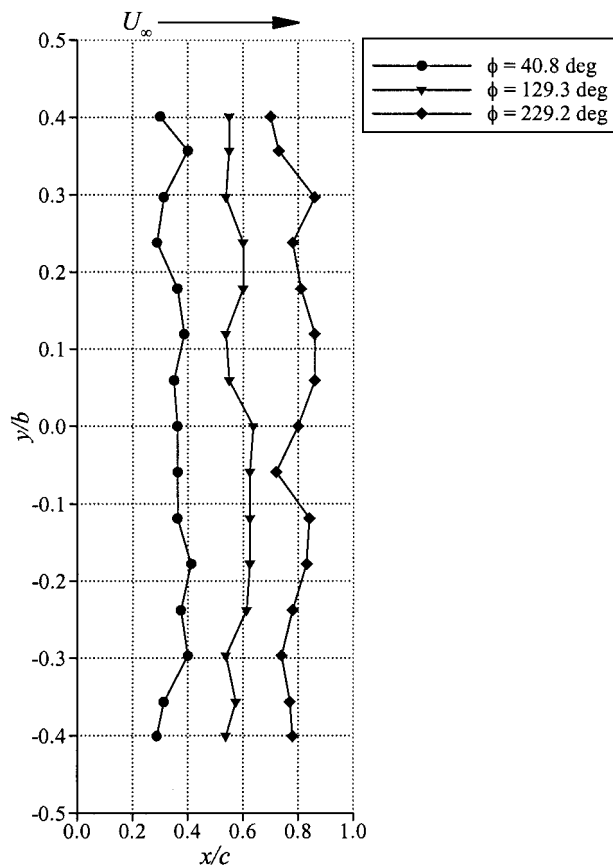

Fig. 11 Spanwise variation in the boundary-layer separation location determined from the conditionally averaged mini-tuft flow visualization for the LRN-1007 airfoil.
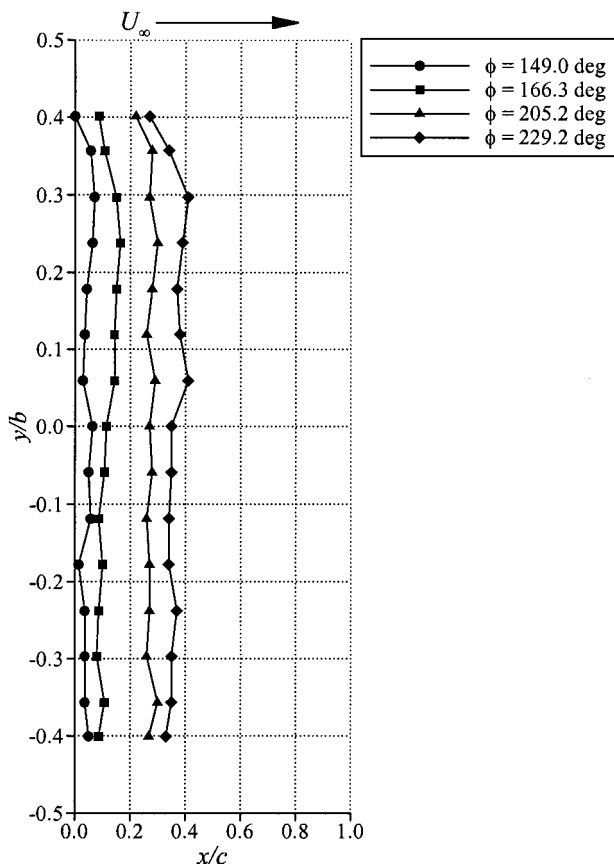
Fig. 12 Spanwise variation in the leading-edge bubble reattachment location determined from the conditionally averaged mini-tuft flow visualization for the LRN-1007 airfoil.

airfoil. The data in Fig. 12 show that the bubble reattachment location progressed downstream with time during the cycle, reaching $x/c \approx 0.35$ for $\phi = 229.2$ deg. This case also corresponds to the farthest downstream location of the boundary-layer separation location in Fig. 11. This complex time-dependent flowfield behavior is considered in more detail in the Discussion. For now, the key conclusion is that the unsteady flow was two-dimensional in the conditionally averaged mean of the fundamental oscillation.

Discussion

Three-Dimensional Structures

The spanwise variation observed for the stalled flowfields on the Ultra-Sport and NACA 2414 airfoils bore strong similarities to stall-cell structures. The work of Winkelmann and Barlow[8] showed that multiple stall cells can occur on three-dimensional models and that the number of stall cells is proportional to the model aspect ratio. In a later study, Yon and Katz[10] used fine-thread-tuft flow visualization on models of variable aspect ratio to further investigate this relationship as well as the unsteady characteristics on the stall-cell patterns. Their model configuration was different in that the ends of the model were fitted with end plates that effectively eliminated the tip flow resulting in more of a two-dimensional configuration. Again, the number of stall cells increased with aspect ratio. However, this trend was offset from the Winkelmann and Barlow[8] data. Yon and Katz[10] attributed the offset to the difference in model end conditions. The latter data are also noteworthy because they showed non-integer numbers of stall cells. For an aspect ratio of 3.0, the number of stall cells was about 1.4. This aspect ratio was very similar to the value of 2.8 for the airfoil models used in the present study.

There were a number of other similarities between the present experiments and those of Yon and Katz.[10] First, for the latter case, the airfoil was a NACA 0015 section and the Reynolds number was 6.2×10^5. The stall-cell patterns were observed over an angle of attack range from 17 to 19 deg, with $\alpha_{stall} = 16$ deg. The authors noted that boundary-layer (trailing-edge) separation was evident approaching α_{stall} prior to the formation of the stall cells.
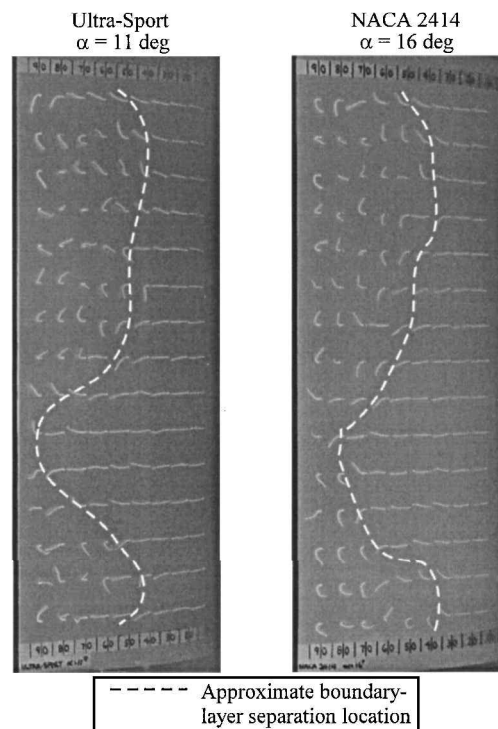

Fig. 13 Mini-tuft flow visualization photographs showing a comparison of boundary-layer separation patterns; flow direction is from right to left.

The symmetric NACA 0015 airfoil is a 15% thick section and at a Reynolds number of 6.2×10^5 it probably exhibited similar characteristics similar to the 14% thick (cambered) NACA 2414 airfoil and the 18% thick Ultra-Sport airfoil, tested at a Reynolds number of 3×10^5. This means that the stall type was probably some combination of trailing-edge and leading-edge stall. The lift data presented in their paper generally confirm this assertion. Another common feature was that all of these airfoils exhibited turbulent boundary-layer (or trailing-edge) separation as the angle of attack was increased to maximum lift.

Based on these comparisons, it is not surprising that the flowfields contained similar characteristics. This is illustrated in Fig. 13, which shows mini-tuft photographs of the Ultra-Sport airfoil at $\alpha = 11$ deg and the NACA 2414 airfoil at $\alpha = 16$ deg. These data were for angles of attack that were about one degree higher than α_{stall}. The separation lines sketched on the photos compared favorably with the sketches shown in Yon[19] for the NACA 0015 airfoil at $\alpha = 17$ deg (e.g., Fig. 2.10). All of the frames showed this noninteger number (approximately 1.4–1.5) of stall-cell patterns. The only substantial difference between the present airfoils and the NACA 0015 is that the boundary-layer separation in the middle of the main stall cell did not extend to the leading edge for the present airfoils.

Yon[19] and Yon and Katz[10] found the noninteger number of stall cells to be "inherently dynamic." That is, the whole stall cell and partial stall cell would intermittently switch places. However, no such behavior was observed in the present tests. The steady stall-cell patterns observed in the present data were confirmed in the wake-velocity data. As noted earlier, the mean velocity was a minimum at the same spanwise location where the boundary-layer separation was a maximum. This was caused by the local enlargement of the wake caused by the stall cell. The combined results of the present data, Yon and Katz, Winkelmann and Barlow, etc., suggest that the stall-cell phenomenon may be related to stall type. A common trend through all of these studies is that they all involved airfoils with trailing-edge or leading-edge stall types or some combination of the two. The present data indicate that the stall behavior for the thin-airfoil and combination thin-airfoil/trailing-edge stall types was fundamentally different.

Yon and Katz[10] performed time-dependent pressure measurements on the airfoil upper surface using a chordwise row of five

high-frequency response pressure transducers. In some cases they recorded frequency components in the fluctuating pressure spectra that converted to Strouhal numbers on the order of 0.040–0.060. These frequencies were only observed when the stall cells were present—for angles of attack greater than α_{stall}. Because of the low values of the Strouhal number, the authors compared their measurements to the low-frequency oscillation of Zaman et al.[1] However, it is clear that these are two different phenomena. The low frequencies measured by Yon and Katz[10] were very low in amplitude, not readily observable in the tuft movement and occurred for angles of attack above maximum lift. In contrast, the low-frequency unsteadiness in the present data was very large in amplitude, clearly observable in the mini-tufts and occurred for angles of attack leading up to and including maximum lift, but generally not above maximum lift. Further, the phase-averaged mini-tuft data and spanwise wake-velocity data showed that the low-frequency flowfield oscillation was primarily two-dimensional in character, markedly different from the stall-cell phenomenon.

Yon and Katz[10] did not suggest that the unsteadiness observed in their stall-cell patterns was identical to the low-frequency oscillation documented by Zaman et al.[1] and the present data. Instead, they speculated that this frequency was associated with large-amplitude motions of the separated shear layer, noted for other cases as shear-layer flapping (e.g., see Driver et al.[20]). It is quite possible that their speculation was indeed correct. Balow[4] suggested that shear-layer flapping was related to the origin of the low-frequency oscillation on the LRN-1007 airfoil. Bragg et al.[5] further speculated that the low-frequency oscillation was symptomatic of a resonance, completed with a "feedback loop" that caused the low-frequency flapping to "lock on" at the low frequency, thus resulting in the quasi-periodic, large-amplitude, stalling, and unstalling behavior. Given these observations, it is possible that the low-frequency measurements of Yon and Katz[10] were related to a shear-layer flapping instability, but the stall cell dominated the flowfield and provided no feedback loop to complete or to lock on this low-frequency fluctuation. Thus, no large-amplitude fluctuations were observed.

The combined results of these investigations suggest that airfoils with trailing-edge separations at and above maximum lift contained these stall-cell patterns, which did not result in the low-frequency oscillation. The present data indicate that these airfoils were of the trailing-edge, leading-edge, and their combination stall-type categories. The airfoils that had leading-edge separation bubbles, which grew in size on the upper surface as the angle of attack was increased into stall, exhibited more two-dimensional flowfield characteristics and low-frequency oscillations. In the combination thin-airfoil/trailing-edge stall case the low-frequency oscillations were very well defined.

More on the Low-Frequency Oscillation

The low-frequency oscillation that occurs during the static stall of the LRN-1007 has been partially illustrated in Figs. 11 and 12. A more complete description of this complex flowfield is provided in Refs. 6 and 7. However, a brief synopsis of these findings is offered here so that the significance of Figs. 11 and 12 can be fully exploited. The LDV measurements from Refs. 6 and 7 provided a quantitative distribution of the streamwise velocity on the LRN-1007 airfoil upper surface conditionally averaged over one oscillation cycle. A time-dependent surface flowfield map is depicted in Fig. 14. The mapping shows the boundary-layer state over the duration of the conditionally averaged cycle. The phase angle ϕ is used to represent the time during the cycle and is identical to the ϕ given in Figs. 11 and 12. The chordwise separation and reattachment locations were obtained from the velocity profiles by extrapolating them to the airfoil surface. Because the flow oscillation is essentially periodic, the starting point was arbitrary and chosen to be $\phi = 15$ deg. At this point in time, the upper-surface boundary layer separates at $x/c = 0.10$. As time increases through the cycle, the boundary-layer separation point progresses toward the trailing edge to about $x/c = 0.80$ at $\phi = 165$ deg. At $\phi = 165$ deg a separation bubble is observed, and its separation and reattachment locations are indicated in Fig. 14 ($x/c \approx 0.05$ and 0.12, respectively). The bubble grows in size from $\phi = 165$ to 255 deg as the bubble separation point moves
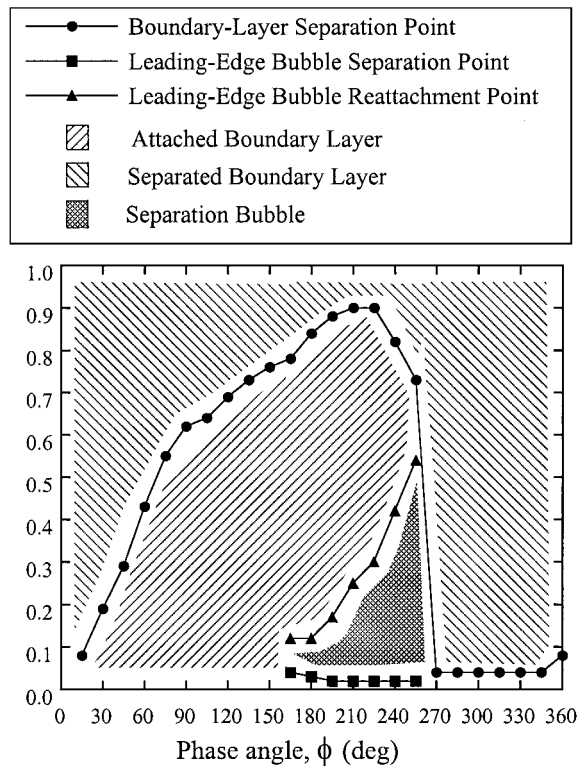
Fig. 14   Variation in the LRN-1007 airfoil upper surface flowfield as a function of phase over the conditionally averaged cycle, after Broeren and Bragg.[7]

slightly forward on the airfoil and the reattachment point moves downstream. Meanwhile, the turbulent boundary-layer separation point continues to progress downstream until $\phi = 225$ deg, where it reverses direction, moving upstream, and ultimately merging with the separation bubble reattachment. Whence this occurs, the entire upper surface boundary layer is separated aft of $x/c \approx 0.05$. The coalescence of the separation bubble reattachment and the trailing-edge separation produces a large region of separated flow on the upper surface from $\phi = 255$ to 360 deg. The boundary-layer separation point remains fixed at $x/c \approx 0.05$. As the boundary-layer separation point begins to move downstream, the oscillation begins again.

Although the previous LDV measurements provided excellent details about the unsteady flow, the velocity field was only measured in a single plane at model midspan. The significance of Figs. 11 and 12 is that they show identical trends to the LDV results and further reveal that the unsteady flow is essentially uniform over the entire span of the model. Not only do the mini-tuft flow visualization results indicate the proper trends, but the absolute values compare favorably as well. For the following comparisons the phase-averaged bubble reattachment and boundary-layer separation locations were averaged over the middle $\frac{1}{3}$ of the span, i.e., $-0.167 < y/b < 0.167$. This interval included data from the midspan mini-tuft row and the first two rows above and below midspan.

The average bubble reattachment and boundary-layer separation locations were plotted as a function of phase angle in Fig. 15. This plot is similar to Fig. 14, without the shaded regions. For $\alpha = 15$ deg these locations corresponded fairly well with the LDV results taken from Fig. 14, further validating the phase-averaged mini-tuft method. The plot also shows that the amount of boundary-layer separation increased with increasing angle of attack, particularly between $\alpha = 14$ and 15 deg. For $\alpha = 16$ deg the boundary-layer separation data were corrupted by the point at $x/c = 0.62$ ($\phi \approx 115$ deg), which was obviously spurious and probably should have been closer to $x/c = 0.50$. The separation bubble was larger for the $\alpha = 15$ deg case over $\alpha = 14$ deg, but both formed at about the same time at $\phi = 140$ deg. The lack of meaningful mini-tuft data later than about $\phi = 240$ deg meant that the flow was completely separated. As just described, this occurred at about $\phi = 255$ deg
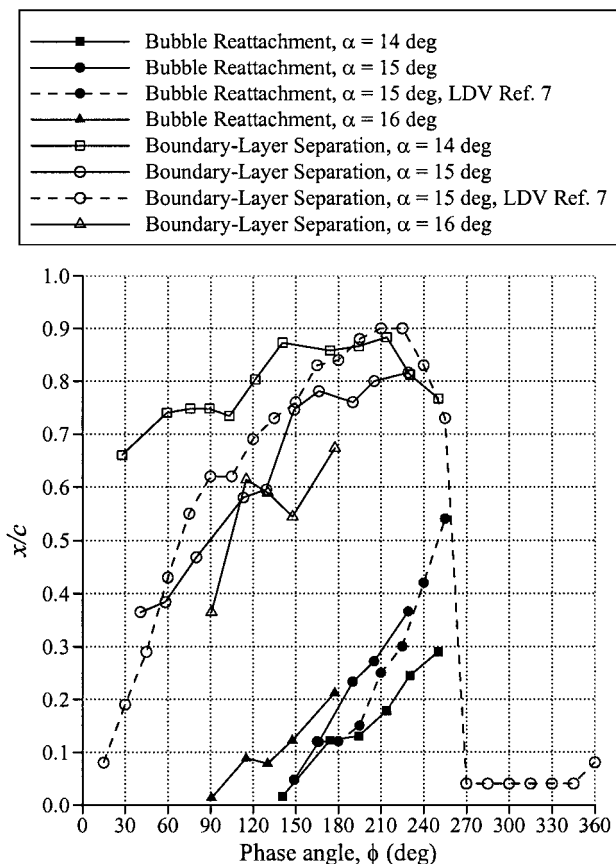
Fig. 15   Variation in the LRN-1007 airfoil upper surface flowfield as a function of phase over the conditionally averaged cycle; present data determined from mini-tuft flow visualization.
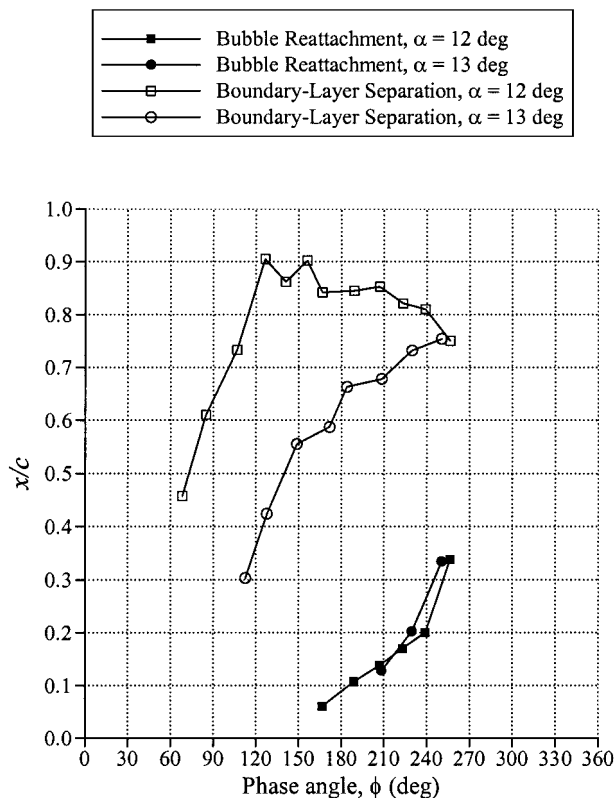

Fig. 16   Variation in the E374 airfoil upper surface flowfield as a function of phase over the conditionally averaged cycle, determined from mini-tuft flow visualization.

(for $\alpha = 15$ deg), when the bubble reattachment point merged with the boundary-layer separation point. A key to this scenario was that the boundary-layer separation location gradually moved downstream until $\phi = 225$ deg, then reversed direction and began moving forward, ultimately merging with the downstream moving bubble reattachment. Similar behavior is shown in Fig. 15 for $\alpha = 14$ deg, as the boundary-layer separation reached a maximum downstream location of about $x/c = 0.88$ at $\phi \approx 215$ deg, then decreased as the bubble continued to grow in size. The data for $\alpha = 16$ deg shows that the bubble was first observed earlier in the oscillation cycle at about $\phi = 90$ deg. However, the bubble did not grow to be as large as in the other cases before the mini-tuft data became uninterpretable. This suggests that the flowfield completely separated earlier in the phase-averaged cycle than at the lower angles of attack.

The unsteady behavior of all of the combination thin-airfoil/trailing-edge stall airfoils tested was found to be very similar. In particular, the E374 airfoil was singled out as having nearly identical unsteady characteristics to the LRN-1007 airfoil. The combined results of the phase-averaged mini-tuft data and the spanwise wake-velocity measurements showed that the low-frequency oscillation was essentially two-dimensional in character on the model surface. Although not explicitly shown here, nearly the same level of spanwise uniformity shown for the LRN-1007 airfoil (Figs. 9–12) was also exhibited by the E374 airfoil, and these data are given by Broeren.[13]

The complementary spanwise-average data for the E374 airfoil (Fig. 16) also showed analogous trends. For this airfoil the separation bubbles were about the same size for both angles of attack. In contrast, there was substantially more turbulent boundary-layer separation at $\alpha = 13$ deg vs $\alpha = 12$ deg until $\phi = 225$ deg. The latter case also showed that the maximum downstream boundary-layer separation location occurred at $x/c = 0.90$ ($\phi = 155$ deg). This location was observed to be coincident with the first appearance of the bubble. This was different from the LRN-1007 airfoil at $\alpha = 14$ deg, where the maximum downstream boundary-layer separation location oc-

curred well after the first appearance of the bubble. The data in Fig. 16 show that the separation bubble was visible on the surface from $\phi = 155$ to 225 deg, which was about 28% of the 360-deg cycle. These data provide even more conclusive evidence that the unsteady flowfields for these two different airfoils were fundamentally identical. This further implies that this low-frequency unsteadiness may be a general phenomenon that occurs for airfoils classified as having a combination thin-airfoil/trailing-edge stall. Even more importantly, it is key flowfield features preceding stall, such as the growing leading-edge separation bubble in tandem with the turbulent boundary-layer separation, that apparently lead to the unsteady flow. Therefore, it is likely that any airfoil exhibiting these features will be characterized by the unsteady stall.

Summary
Several airfoils having different stalling characteristics were studied to better understand the unsteady and three-dimensional flowfield variations governing the stall. The airfoils were tested in a two-dimensional configuration where the ends of the models were flush with the wind-tunnel side walls. Wake-velocity measurements and surface mini-tuft flow visualization were carried out at a Reynolds number of 3×10^5. The results showed that the stall of airfoils having trailing-edge separation leading up to the stall was characterized by large-scale spanwise structures similar to stall cells. The stall cells were observed on the airfoil upper surface for angles of attack at or above stall (maximum lift) and were generally steady. Conversely, the stall of airfoils having a thin-airfoil or combination thin-airfoil and trailing-edge stall type, where a leading-edge separation bubble grows in size leading up to the stall, was governed by low-frequency unsteady flow. This unsteady flow generally occurred prior to and including the mean maximum lift region. The flowfield was found to be two-dimensional in the conditionally averaged mean of the oscillation, with no evidence of stall cell formation. Therefore, these appear to be exclusive phenomena that are determined by the boundary-layer separation characteristics leading up to the stall, which depend on the airfoil geometry (i.e., the pressure distribution).

Acknowledgments

References

[1]Zaman, K. B. M. Q., McKinzie, D. J., and Rumsey, C. L., "A Natural Low-Frequency Oscillation over Airfoils near Stalling Conditions," *Journal of Fluid Mechanics*, Vol. 202, 1989, pp. 403–442.

[2]Bragg, M. B., Heinrich, D. C., and Khodadoust, A., "Low-Frequency Flow Oscillation over Airfoils near Stall," *AIAA Journal*, Vol. 31, No. 7, 1993, pp. 1341–1343.

[3]Heinrich, D. C., "An Experimental Investigation of a Low Frequency Flow Oscillation over a Low Reynolds Number Airfoil near Stall," M.S. Thesis, Dept. of Aeronautical and Astronautical Engineering, Univ. of Illinois, Urbana, IL, 1994.

[4]Balow, F. A., "Effect of an Unsteady Laminar Separation Bubble on the Flowfield over an Airfoil near Stall," M.S. Thesis, Dept. of Aeronautical and Astronautical Engineering, Univ. of Illinois, Urbana, IL, 1994.

[5]Bragg, M. B., Heinrich, D. C., Balow, F. A., and Zaman, K. B. M. Q., "Flow Oscillation over an Airfoil near Stall," *AIAA Journal*, Vol. 34, No. 1, 1996, pp. 199–201.

[6]Broeren, A. P., "Phase-Averaged LDV Flowfield Measurements About an Airfoil in Unsteady Stall," M.S. Thesis, Dept. of Mechanical and Industrial Engineering, Univ. of Illinois, Urbana, IL, 1996.

[7]Broeren, A. P., and Bragg, M. B., "Flowfield Measurements over an Airfoil During Natural Low-Frequency Oscillations near Stall," *AIAA Journal*, Vol. 37, No. 1, 1999, pp. 130–132.

[8]Winkelmann, A. E., and Barlow, J. B., "Flowfield Model for a Rectangular Planform Wing Beyond Stall," *AIAA Journal*, Vol. 18, No. 8, 1980, pp. 1006–1008.

[9]Winkelmann, A. E., "Flow Field Studies Behind a Wing at Low-Reynolds Numbers," AIAA Paper 90-1471, June 1990.

[10]Yon, S. A., and Katz, J., "Study of the Unsteady Flow Features on a Stalled Wing," *AIAA Journal*, Vol. 36, No. 3, 1998, pp. 305–312.

[11]Kline, S. J., and McClintock, F. A., "Describing Uncertainties in Single-Sample Experiments," *Mechanical Engineering*, Vol. 75, Jan. 1953, pp. 3–8.

[12]Coleman, H. W., and Steele, W. G., *Experimentation and Uncertainty Analysis for Engineers*, Wiley, New York, 1989, pp. 40–118.

[13]Broeren, A. P., "An Experimental Study of Unsteady Flow over Airfoils near Stall," Ph.D. Dissertation, Dept. of Mechanical and Industrial Engineering, Univ. of Illinois, Urbana, IL, 2000.

[14]Crowder, J. P., "Flow Visualization," *The Handbook of Fluid Dynamics*, edited by R. W. Johnson, CRC Press, Boca Raton, FL, 1998, pp. 38-1–38-42.

[15]Broeren, A. P., and Bragg, M. B., "Low-Frequency Flowfield Unsteadiness During Airfoil Stall and the Influence of Stall Type," *Proceedings of the 16th Applied Aerodynamics Conference*, AIAA, Reston, VA, 1998, pp. 196–209.

[16]Broeren, A. P., and Bragg, M. B., "Unsteady Stalling Characteristics of Thin Airfoils at Low-Reynolds Number," *Proceedings of the Conference on Fixed, Flapping and Rotary Vehicles at Very Low Reynolds Number*, edited by T. J. Mueller, Univ. of Notre Dame, Notre Dame, IN, 2000, pp. 396–420.

[17]McCullough, G. B., and Gault, D. E., "Examples of Three Representative Types of Airfoil-Section Stall at Low-Speed," NACA TN 2502, Sept. 1951.

[18]Selig, M. S., Guglielmo, J. J., Broeren, A. P., and Giguere, P., "Experiments on Airfoils at Low-Reynolds Numbers," AIAA Paper 96-0062, Jan. 1996.

[19]Yon, S. A., "Coherent Structures in the Wake of a Stalled Rectangular Wing," Ph.D. Dissertation, Dept. of Applied Mechanics, Univ. of California, San Diego, CA, and College of Engineering, San Diego State Univ., San Diego, CA, 1995.

[20]Driver, D. M., Seegmiller, H. L., and Marvin, J., "Time-Dependent Behavior of Reattaching Shear Layers," *AIAA Journal*, Vol. 25, No. 7, 1987, pp. 914–919.

A. Plotkin
Associate Editor